

Tectonics

RESEARCH ARTICLE

10.1029/2021TC006740

Key Points:

- CA-SA relative plate motion is partitioned along the transform boundary on multiple fault segments
- Plate boundary faults are locked west of 64°W, while faults to the east are creeping, except the Sub-Tobago Terrane fault
- The western segment of the plate boundary could produce a M_w 8 earthquake

Supporting Information:

Supporting Information may be found in the online version of this article.

Correspondence to:

M. Higgins,
mhh16@psu.edu

Citation:

Higgins, M., La Femina, P. C., Weber, J. C., Geirsson, H., Ryan, G. A., & Wauthier, C. (2021). Strain partitioning and interseismic fault behavior along the Caribbean-South American transform plate boundary. *Tectonics*, 40, e2021TC006740. <https://doi.org/10.1029/2021TC006740>

Received 23 JAN 2021

Accepted 8 JUL 2021

© 2021. American Geophysical Union.
 All Rights Reserved.

Strain Partitioning and Interseismic Fault Behavior Along the Caribbean-South American Transform Plate Boundary

M. Higgins¹ , P. C. La Femina¹ , J. C. Weber² , H. Geirsson³ , G. A. Ryan^{4,5}, and C. Wauthier¹ 

¹Department of Geosciences, The Pennsylvania State University, University Park, PA, USA, ²Department of Geology, Grand Valley State University, Allendale, MI, USA, ³Institute of Earth Sciences, University of Iceland, Reykjavik, Iceland, ⁴Seismic Research Center, University of the West Indies, St. Augustine, Trinidad and Tobago, ⁵Montserrat Volcano Observatory, Flemmings, Montserrat

Abstract We combine Global Positioning System and Interferometric Synthetic Aperture Radar (InSAR) data to characterize the interseismic behavior (i.e., locked or creeping), and strain partitioning for the faults along the Caribbean-South American transform plate boundary. Interseismic strain is distributed mainly on three faults, the San Sebastian, El Pilar, and Central Range faults, but partitioning occurs across multiple faults in the west (San Sebastian and La Victoria faults) and east (Sub-Tobago Terrane, Central Range, and South Coast faults). In northern Venezuela, slip is partitioned on the San Sebastian (16.4 ± 1.7 mm/yr) and La Victoria (4.3 ± 0.9 mm/yr) faults. In north-eastern Venezuela, the El Pilar fault accommodates slip at a rate of 18.6 ± 1.8 mm/yr. In Trinidad and Tobago, slip is partitioned between the Sub-Tobago Terrane (3.0 ± 0.1 mm/yr), Central Range (14.5 ± 2.0 mm/yr), and South Coast (3.0 ± 0.1 mm/yr) faults. The La Victoria, San Sebastian, the western El Pilar segment, and Sub-Tobago Terrane faults are locked to depths of 16.2 ± 4.0 km, 7.7 ± 5.2 km, 6.7 ± 2.8 km, and 8.0 ± 0.2 km, respectively. The eastern segment of the El Pilar, the Central Range, and the South Coast faults all creep. Our new InSAR results indicate that the entire Central Range Fault is creeping. The locked western segment of this transform plate boundary is capable of producing a M_w 8 earthquake, which is a significant finding regarding seismic hazard and risk.

1. Introduction

Continental transform plate boundaries can be complex deformation zones with multiple faults accommodating relative plate motion. The Pacific-North American plate boundary is a complex continental transform system dominated by the San Andreas fault, but with at least five major overlapping faults in the south, and three faults in the north (e.g., Lisowski et al., 1991). The North Anatolian fault system also displays along-strike complexities (Bohnhoff et al., 2006; Şengör et al., 2005). The faults that comprise continental transform fault systems can also have variable interseismic behavior, varying from completely locked to creeping at full relative plate motion rate.

Fault systems such as the San Andreas (Maurer & Johnson, 2014; Savage & Burford, 1973; Titus et al., 2006), the North Anatolian (Bilham et al., 2016; Cetin et al., 2014), and the Haiyuan (Cavalié et al., 2008; Jolivet et al., 2012) each have segments that together display this full spectrum of interseismic behavior, with earthquakes occurring in not only the locked segments but also in the creeping segments or in transition zones between locked and creeping segments (Bakun et al., 2005; Gans et al., 2003; Wallace, 1970; WGCEP, 2003).

The Caribbean (CA)-South American (SA) transform plate boundary zone demonstrates the characteristics of variable along-strike strain partitioning and the complete spectrum of interseismic fault behavior (Pérez et al., 1997, 2001, 2018; Reinoza et al., 2015; Weber et al., 2011, 2020). The dextral transform boundary is comprised of three main fault systems: (a) the San Sebastian (SSF) and La Victoria (LVF) faults (Schubert, 1981; Schubert & Krause, 1984); (b) the El Pilar fault (EPF) (Molnar & Sykes, 1969; Pérez et al., 2001; Russo & Speed, 1992; Russo et al., 1993; Speed, 1985); and (c) the Central Range (CRF), South Coast (SCF), and Sub-Tobago Terrane (STTF) faults (Figure 1) (Weber, 2010; Weber et al., 2001, 2020). These fault systems accommodate the ~ 21 mm/yr of CA-SA relative motion (DeMets et al., 2010; Symithe et al., 2015), and display variable historical seismicity along strike (e.g., Audemard, 2007; Baumbach et al., 2004; Pérez

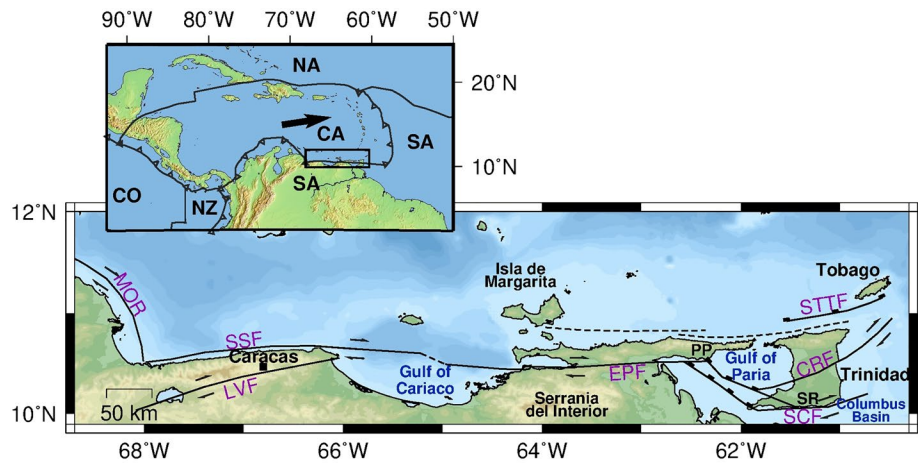


Figure 1. Active faults of the southeastern Caribbean-South American transform plate boundary. MOR, Morrocoy Fault; SSF, San Sabastian Fault; LVF, La Victoria Fault (Pérez et al., 1997); EPF, El Pilar Fault; CRF, Central Range Fault Zone; SC, South Coast Fault; and STTF, Sub-Tobago Terrane Fault (Robertson & Burke, 1989; Soto et al., 2007; Weber et al., 2020). Region names: SDI, Serrania del Interior; PP, Paria Peninsula; and SR, Southern Range. Bathymetry and topography are from ETOPO1 (Amante & Eakins, 2009). Inset shows tectonic setting around the Caribbean plate (CA, Caribbean plate; CO, Cocos plate; NZ, Nazca plate; NA, North American plate; and SA, South American plate) with black box identifying the region of study and black arrow showing the direction of CA motion relative to SA at our region of study.

et al., 1997). To determine its seismic potential, it is essential to resolve how strain is partitioned and how interseismic strain accumulates on faults along this boundary.

We combine Global Positioning System (GPS) and Interferometric Synthetic Aperture Radar (InSAR) data, to evaluate for the first time, interseismic fault behavior (i.e., the magnitude and location of interseismic strain and locking depth) along the entire CA-SA transform plate boundary. We comprehensively quantify the modes of interseismic behavior, including elastic strain accumulation and partitioning along strike, compare our geodetic model results to the pattern and magnitude of historical seismic moment release, and attempt to correlate fault behavior to geology.

2. Active Faults and Geology of the CA-SA Transform Plate Boundary

The CA-SA transform plate boundary is composed of three faults systems with six faults that accommodate the ~21 mm/yr of relative CA-SA dextral shear (Figure 1). In the following sections, we give detailed descriptions of these faults and their historical seismicity, results of previous geodetic studies, and describe how the geology changes along the plate boundary.

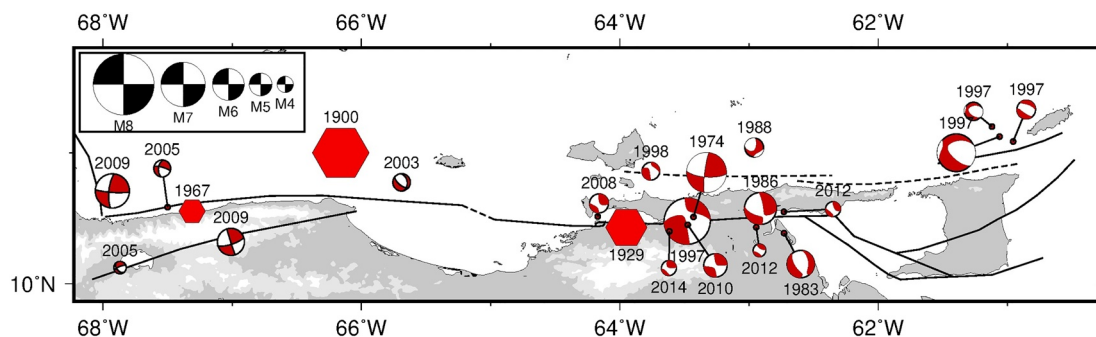


Figure 2. Shallow seismicity (<30 km) with magnitude 3.5 or greater labeled with the year of occurrence above or below the symbol (see Tables S.1 and S1.2). Focal mechanisms are from the GCMT (Dziewonski et al., 1981; Ekström et al., 2012) and International Seismological Centre (ISC, Lentas, 2017; Lentas et al., 2019) catalogs with locations from the ISC published catalog (Storchak et al., 2015). Focal mechanism for 1974 (M6.1) earthquake from Russo and Speed (1994). Hexagons are earthquakes from the ISC catalog and the Centennial Earthquake Catalog (Engdahl et al., 2013) except for the 1929 Cumana earthquake (Mocquet et al., 1996). Black lines are major faults of the region of study (see Figure 1 for details).

2.1. San Sebastian and La Victoria Faults

The E-W trending SSF and the WSW-ENE trending LVF accommodate ~90% of the CA-SA motion (i.e., ~19 mm/yr) in the western segment of the plate boundary in north-central Venezuela (Figure 1) (Pérez et al., 2018; Schubert, 1981). The SSF has a fairly simple 280 km long fault trace (Colón et al., 2015; Escalona et al., 2011; Schubert & Krause, 1984), and connects to the western EPF across the Gulf of Cariaco pull-apart basin (Escalona et al., 2011; Schubert, 1985). The LVF has a 230 km long trace and terminates in the Gulf of Cariaco (Schubert & Krause, 1984).

The SSF and LVF have produced intermediate to large magnitude earthquakes (Table S1.1). The SSF ruptured during the September 12, 2009 M_w 6.1, the damaging 1967 M 6.5 Caracas (Pérez, 1998a; Suárez & Nábělek, 1990), and the 1900 M 7.6 to M 8.0 earthquakes, where the latter ruptured the eastern SSF segment (Figure 2; Colón et al., 2015; Pacheco & Sykes, 1992). Microseismicity ($M \leq 4$) has been detected on the SSF, with a greater number of events on its eastern segment than on its central and western segments (Pérez et al., 1997). The LVF has had several moderate magnitude earthquakes, including several earthquakes with magnitudes greater than M 6 (e.g., 1641 and 1878) (Pérez, 1998b; Pérez et al., 1997).

There has been only one geodetic study of the interseismic behavior of the SSF and LVF. Pérez et al. (2018) inverted episodic GPS-derived horizontal velocities and found that the SSF and LVF accommodate 17.0 ± 0.8 mm/yr and 2.1 ± 0.8 mm/yr, respectively, and are locked to a depth of 14 km.

2.2. El Pilar Fault

The E-W trending EPF accommodates ~85% of the CA-SA motion (i.e., ~18 mm/yr) in the central section of the plate boundary (Beltran et al., 2016; Jouanne et al., 2011; Pérez et al., 2001; Reinoza et al., 2015), and four along-strike segments have been mapped. From west to east these are: (a) a 100 km-long segment from the Gulf of Cariaco pull-apart to a restraining bend at the city of Cumana (Escalona et al., 2011; Lidz et al., 1968); (b) an 80 km long linear segment from Cumana to the Casanay restraining bend (Beltran et al., 1996); (c) a 45 km long linear segment from the Casanay restraining bend to the town of El Pilar (Beltran et al., 1996); and (d) the easternmost 65 km-long segment that terminates in the Gulf of Paria pull-apart basin (Beltran et al., 1996; Flinch et al., 1999; Speed, 1985). EPF segmentation was further highlighted by analysis of aftershocks from the 1997 Cariaco earthquake (Figure 2). Baumbach et al. (2004) found six micro-segments, corresponding to previously described segments 2, 3, and 4, and surface ruptures were observed that correspond to segments 2 and 3 (Audemard, 2006).

The EPF is historically the most seismically active of all the faults in the plate boundary (Figure 2; Table S1.2). It has experienced multiple intermediate to large magnitude earthquakes in modern times, with the largest being the 1997 M_w 6.8 Cariaco (Mendoza, 2000; Pérez, 1998a) and the 1929 M 6.5 Cumana earthquakes (Figure 2; Mocquet et al., 1996). The western segment of the EPF had an intermediate magnitude, possibly $>M$ 6.5, earthquake in 1797 (Audemard, 2007); however, there are no earthquakes recorded on this segment during instrumented times (Figure 2). The eastern segment of the EPF has $>M$ 5 earthquakes regularly (i.e., approximately every 2 years), as well as larger magnitude earthquakes (International Seismological Centre [ISC] catalog; Storchak et al., 2015, 2017). Damaging historical earthquakes (e.g., 1684) have also been associated with this segment (Audemard, 2007).

Given the record of frequent seismicity and the disparate geology across the fault (Jordan, 1975; Schubert, 1979), the EPF was one of the first transform faults identified and therefore much work has focused on this segment of the plate boundary. Previous geodetic studies characterized the interseismic slip rate and locking depth of the EPF. Pérez, et al. (2001) used local and regional episodic GPS data (1994, 1999, and 2000) to model an interseismic locking depth of 14 km for the entire EPF. Reinoza et al. (2015) used a more expansive GPS network and inverted continuous and episodic GPS data (from observations taken in 2003, 2005, and 2013) along the EPF using a suite of modeling methods. First, the authors projected GPS velocity data from the entire 240 km length of the fault system and width of their geodetic network onto one fault-normal profile. They then inverted those data using the method of Savage and Burford (1973) and found a locking depth of 1.6 km. Second, the authors used a distributed-slip model (Wang et al., 2013) to determine the interseismic slip deficit and locking on discretized fault patches (patch sizes of 4 km^2) along the strike of the EPF. The results of this model indicated that there is an EPF fault patch west of Cumana with

partial slip (10 mm/yr to 12 mm/yr relative to plate motion) and that all other segments creep at the plate motion rate. Finally, Beltran et al. (2016) used InSAR time-series analysis of 18 ALOS-1 synthetic aperture radar data to study aseismic creep on the eastern EPF between 2007 and 2011. These authors found that the rate of creep decreased from $\sim 25 \pm 9.5$ mm/yr (i.e., 4 mm/yr faster than the relative plate rate) in the west (63.7°W) to $\sim 13 \pm 6.9$ mm/yr in the east (63.3°W).

2.3. Sub-Tobago Terrane, Central Range, and South Coast Faults

CA-SA relative motion is partitioned between three faults at the longitude of Trinidad-Tobago. From north to south these are: the Sub-Tobago Terrane (STTF), Central Range (CRF), and South Coast (SCF) (Figure 1; Weber et al., 2020). The STTF is seismically active and has ruptured during several moderate magnitude earthquakes, including the 1997 M_w 6.7 Tobago, which was a dextral oblique-slip earthquake (Weber et al., 2015). The CRF cuts through central Trinidad with a strike of $\sim 070^\circ$, roughly aligned with CA-SA relative plate motion (Flinch et al., 1999; Weber et al., 2020 and references therein). The western onshore portion of the CRF is aseismically creeping and separates rocks with a thermogenic petroleum charge to its south, from those with only dry biogenic gas to the north (Weber et al., 2020 and references therein). Weber et al. (2020) suggested that overpressured hydrocarbons and weak fault gouge result in aseismic creep on the western CRF. Before our current study, slip on the eastern segment of the CRF had not been previously quantified.

The E-W trending SCF spans the entire length of the south coast of Trinidad and separates the onshore Southern Range from the Columbus Basin, an active extensional province (Erlich & Barrett, 1990; Garcicaro et al., 2011; Pindell & Kennan, 2001). The seismic behavior on the SCF is not well known; no historical earthquakes have been associated with this fault. However, the fault is thought to be creeping at ~ 3 mm/yr based on analysis of geodetic data (Weber et al., 2020), and abundant evidence for overpressured fluids, including the presence of fault-aligned and deeply rooted mud volcanoes (Deville & Guerlais, 2009; Henry et al., 2010; Heppard et al., 1998; Higgins & Saunders, 1967).

Previous work using geodesy to investigate the earthquake hazard of the CRF and partitioning of plate boundary strain across Trinidad-Tobago has mainly been carried out by Weber (2010) and Weber et al. (2001, 2011, 2020). This body of work demonstrates that the CRF accommodates $\sim 70\%$ of the CA-SA motion (13–14 mm/yr) and is creeping, while the STTF and SCF each accommodates ~ 3 mm/yr. Weber et al. (2020) found this slip partitioning using a GPS network that formed a fault normal profile across the western CRF. The network lacked the spatial resolution to determine variation in locking along strike. We improve upon these studies here with expanded spatial resolution by combining GPS and InSAR data sets.

2.4. Geology of CA-SA Transform Boundary

The CA-SA boundary is geologically complex, owing to several phases of tectonic development. The current crustal geology is associated with rifting during the Cretaceous breakup of Pangea (Stockhert, 1995), Paleogene oblique convergence between CA and SA (Pindell & Barrett, 1990; Speed, 1985), and Pliocene to present eastward translation of the CA plate (Boschman et al., 2014; Burke, 1988). We divide the geology here into five principal tectonostratigraphic units (Figure 3). The SSF and LVF together bound the Caracas-Araya-Margarita unit which is comprised of high-grade, blueschist-bearing metamorphic rocks that experienced Cretaceous metamorphism, likely in a subduction zone (Sisson et al., 2005, 1997; Sorensen et al., 2005). The Caucauga-El Tinaco-Paracotos (CTP) unit, south of the LVF, is an ophiolite-bearing metamorphic complex with variable protolith and metamorphic ages and a wide variety of metamorphic rock types (Ostos & Sisson, 2005; Ysaccis, 1998). The Villa de Cura unit, located south of the CTP, is a thrust-bounded (klippe) accreted Cretaceous arc, part of Burke (1988) Great Arc of the Caribbean, the geology of which correlates with units in Tobago and the Leeward Antilles (Maresch, 1974; Ostos & Sisson, 2005; Ysaccis, 1998). Low-grade metasedimentary rocks (e.g., schist, marble, quartzite), that were metamorphosed and exhumed in the Cenozoic, crop out in the Paria Peninsula in northeastern Venezuela and in Trinidad's Northern Range (Avé Lallemand, 1997; Cruz et al., 2007; Weber et al., 2001). South of the metamorphic units, the South American passive margin, and foreland sedimentary fill sequence

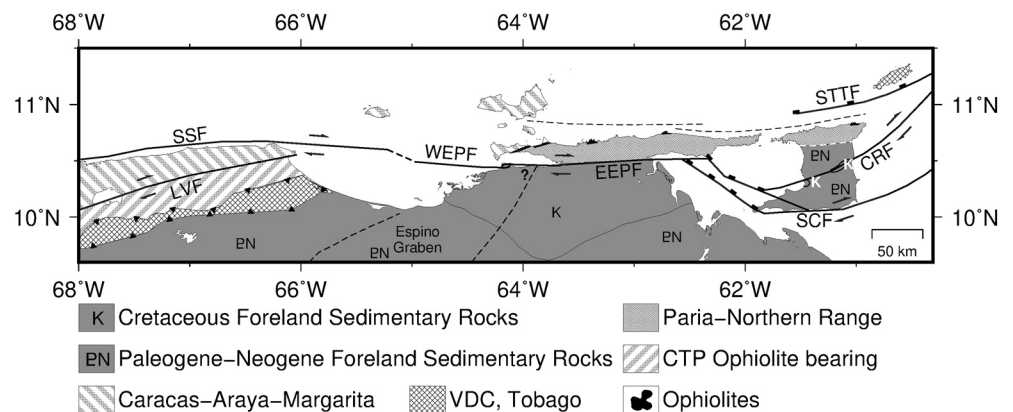


Figure 3. Bedrock geological map showing principal tectonostratigraphic units in the CA-SA transform boundary (Modified from Avé Lallemant & Sisson, 2005; French & Schenk, 2004). Quaternary deposits are omitted. PN and K, foreland and passive margin sedimentary units of Paleogene-Neogene and Cretaceous age, respectively. Espino Graben, Jurassic subsurface structure. CTP, ophiolite-bearing rocks of Caucaquia-El Tinaco and Paracotos belts. VDC, Villa de Cura Nappe. Fault names in large fonts are: SSF, San Sebastian Fault; LVF, La Victoria Fault; WEPF, western El Pilar Fault segment; EEPF, eastern El Pilar Fault segment; CRF, Central Range Fault Zone; SCF, South Coast Fault; and STTF, Sub-Tobago Terrane Fault.

consists of and exposes both Cretaceous (e.g., the Serrania del Interior and central Trinidad), and younger Paleogene-Neogene rocks (Figure 3). The Espino Graben is a Jurassic-aged subsurface feature related to Pangea breakup that is known primarily from oil and gas drilling and exploration (Garcia-Abdeslem et al., 2013).

3. Data

To explore the interseismic behavior of the southern CA-SA transform plate boundary, we use both geodetic and earthquake data. We unify published GPS velocity vectors, newly analyzed continuous GPS (cGPS), and ALOS-2 Synthetic Aperture Radar (SAR) data to characterize interseismic strain accumulation along the entire ~900 km length of the plate boundary. To determine the seismic moment released along the plate boundary we use the reviewed ISC catalog (Storchak et al., 2015, 2017).

3.1. Global Positioning System Data

We use GPS velocities in the ITRF2008 reference frame to study: (a) SSF and LVF (8 GPS stations; Pérez et al., 2018), EPF (33 GPS stations; Reinoza et al., 2015), and STTF, CRF, and SCF (19 GPS stations; Weber et al., 2020) (Figure 4; Tables S2.1); and (b) data from 11 cGPS stations, which extends time series, improving precision and accuracy, for stations presented in Weber et al. (2020) (Figure 4; Tables S2.1 and S2.2). GPS analysis followed the methods of Weber et al. (2020). Analysis of the cGPS daily position time series, including the estimation of seasonal signals, velocities, and uncertainties, was performed using the HECTOR software (Bos et al., 2013).

Our new horizontal GPS velocity field (60 stations; Table S2.1; Figure 4) was then transformed from ITRF2008 into a SA reference frame (Kreemer et al., 2014). The velocity field clearly shows a transition from SA to CA motion across the SSF, EPF, and CRF, with most vectors aligned with the azimuth of CA relative motion (Figure 4). Velocities south of the LVF tend to SA motion (i.e., ~0.0 mm/yr). Residual velocities of up to 3 mm/yr, south of the EPF have no clear agreement in azimuth. We use this new horizontal velocity field to investigate the interseismic nature of the CA-SA plate boundary, including interseismic strain accumulation, creep, and locking depths on the main active faults in this region in Section 4.

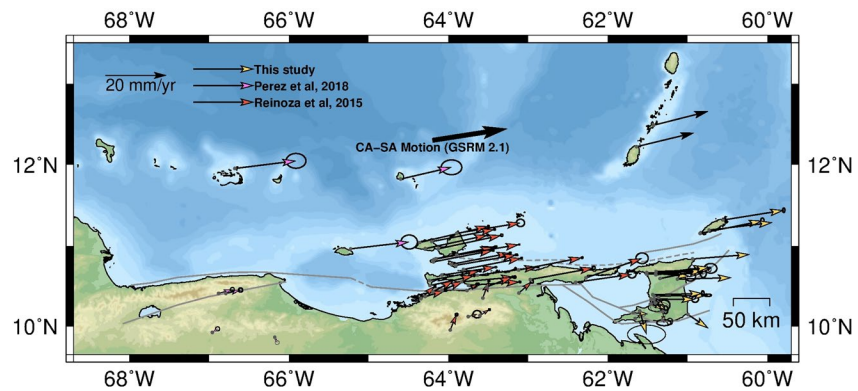


Figure 4. Global Positioning System (GPS) velocities in the ITRF2008 South America-fixed reference frame (Kreemer et al., 2014). Violet- and red-tipped velocity vectors are from Pérez et al. (2018) and Reinoza et al. (2015), respectively. Only seven of the eight GPS velocities from Pérez et al. (2018) are plotted, the eight is off the map. Yellow-tipped velocity vectors are updated GPS data from Weber et al. (2020). Black velocity vectors are GPS velocities from this study but not used in modeling. Large black vector shows the relative motion (~ 21 mm/yr) of CA with respect to SA (Kreemer et al., 2014). Major faults are shown as thin gray lines.

3.2. Interferometric Synthetic Aperture Radar Data

We use Interferometric Synthetic Aperture Radar (InSAR) to investigate tectonic displacement on the island of Trinidad, by utilizing Synthetic Aperture Radar (SAR) scenes from the PALSAR-2 sensor (wavelength of 23 cm) onboard the ALOS-2 satellite. L-Band SAR (wavelength of 15–30 cm) has the ability to penetrate the tropical broadleaf vegetation found in this region (Wei & Sandwell, 2010). We chose not to use SAR scenes from the L-band ALOS-1, the predecessor of the ALOS-2 mission, because of large perpendicular baselines (>300 m) between scenes and the resulting poor coherence interferograms for this region. We used nine ALOS-2 SAR scenes (path 36, frame 200), with acquisition dates from February 4, 2015 to March 27, 2019 (4.14 years).

ALOS-2 SAR scenes were processed and co-registered to a primary scene using the GMTSAR software package (Sandwell et al., 2016). Nineteen interferometric pairs with perpendicular baselines less than 300 m and temporal baselines less than 600 days were created. The 19 interferometric pairs were unwrapped by first masking out water bodies and low coherence pixels and interpolating the remaining phases with the nearest-neighbor approach, and using the minimum spanning tree algorithm implemented in the SNA-PHU software (Chen & Zebker, 2000, 2002). Interferograms with orbital error trends were detrended by identifying the planar trend by least squares fitting and removing the resulting trend. The coherence-based small-baseline subset algorithm (SBAS) was then used in calculating the time series of the scenes and the velocities of pixels in the scenes (Berardino et al., 2002; Schmidt & Bürgmann, 2003; Tong & Schmidt, 2016; Xu et al., 2017). SBAS derived velocities were further detrended to remove long-wavelength planar trends (Figure S5.5).

3.3. Earthquake Data

We use epicenter location and magnitude data from the ISC reviewed catalog (Storchak et al., 2015, 2017) to determine the seismic moment released on the plate boundary. The catalog incorporates data from local seismic observatories (i.e., Fundación Venezolana de Investigaciones Sismológicas and the University of the West Indies, Seismic Research Centre), as well as that from global seismic networks. Therefore this catalog is more complete at a regional scale for low- to moderate-magnitude earthquakes than other global catalogs (Willemann & Storchak, 2001). The catalog includes 1,881 earthquakes from 1927 to 2017 with hypocenter depths of 20 km or less, in the region from latitude 8.5°N to 12°N and longitude 60.0°W to 68.0°W .

4. Modeling Methods

We use the elastic dislocation model of Savage and Burford (1973) to investigate interseismic fault behavior (locked and accumulating strain vs. creeping), locking depth, and strain partitioning along the entire ~900 km CA-SA transform plate boundary for the very first time. We model the GPS and InSAR (CRF only) derived fault-parallel velocities for each of the three fault systems: (a) SSF and LVF; (b) EPF; and (c) STTF, CRF, and SCF, by projecting horizontal velocities onto the strike of one fault in each fault system. For the SSF and LVF and the STTF, CRF, and SCF fault systems, our modeling strategy treats these faults as subparallel, even though their strikes differ by a maximum of 11°. The difference in strikes is equivalent to no greater than a 6% change in projected velocities, which is within the uncertainty (~1.5 mm/yr) of the observed GPS velocities. To estimate parameter uncertainties and to avoid local minima, we implemented a Monte Carlo (MC) inversion scheme. The MC method perturbed the datasets by randomly sampling within the $\pm 1\sigma$ error of the original velocities. The modeling treatment of each fault system is described in the following sections.

4.1. San Sebastian and La Victoria Faults

For modeling of the interseismic slip deficits and locking depths of the SSF and LVF, we assumed the faults were parallel and used SSF fault-parallel velocities. We chose the across-strike distance of the SSF and LVF to be 0 km and -47 km, respectively, following Pérez et al. (2018). To test the effect of low velocity uncertainties for stations south of the SSF (Figure 4), we incorporated a hybrid bootstrap method, randomly selecting and removing one station before inversion. A full bootstrapping method could not be employed given the small number (8) of data points.

4.2. El Pilar Fault

To investigate along-strike changes in interseismic slip deficit and locking depth on the previously described segments of the EPF, we modeled velocity profiles that were normal to the fault. First, we modeled evenly spaced velocity profiles along the entire length of the fault zone (Section S4), which guided our choice to model three profiles (i.e., profiles A, B, and C; Figure 5) selected to capture the separate segments of the EPF and its important transition from locking to creeping (Figures S4.1, S4.2 and Table S4.1). Profile A captures the western 55 km of the EPF (previously described segment 1), which has a significant locking

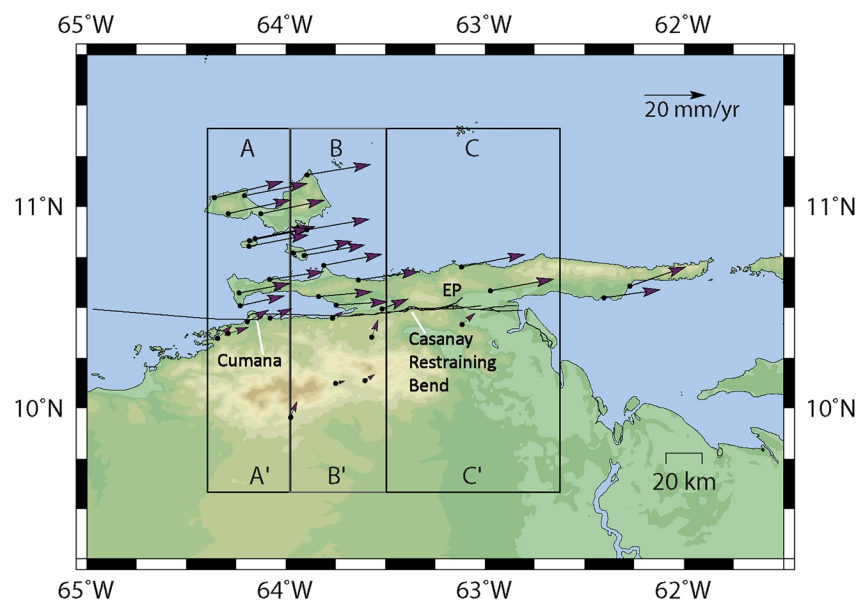


Figure 5. Global Positioning System velocity profile locations A, B, and C for the El Pilar fault (EPF). EP, the town of El Pilar, which corresponds to the easternmost extent of EPF segment 4.

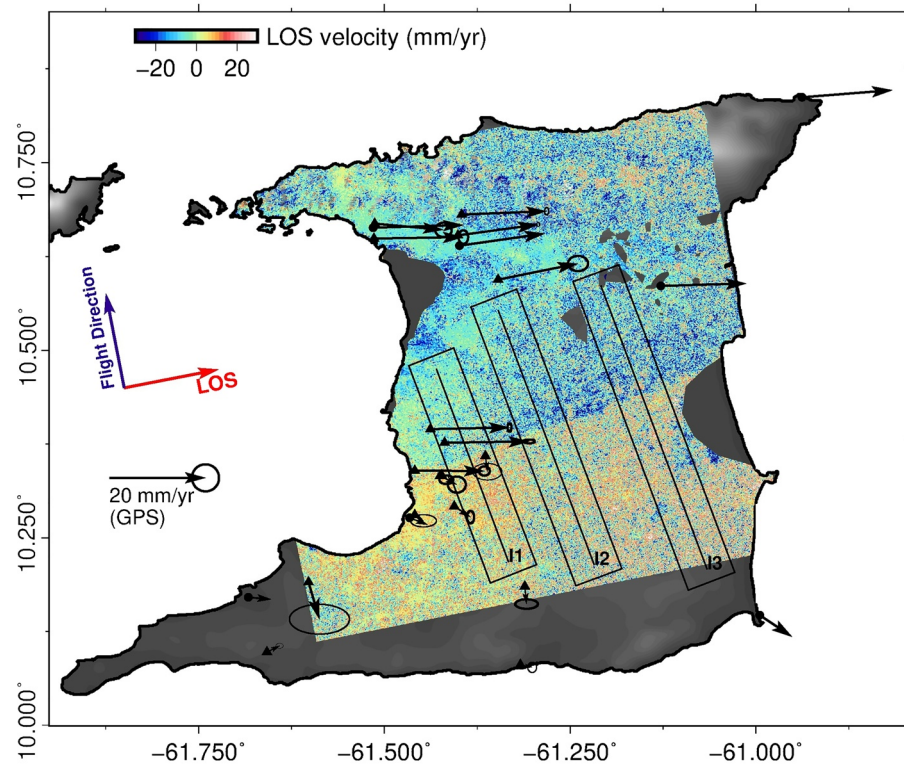


Figure 6. ALOS-2 line-of-sight velocity field in mm/yr calculated using the small-baseline subset algorithm method. Horizontal Global Positioning System (GPS) velocity vectors as in Figure 4, where circle icons are cGPS stations and triangle icons are episodic GPS stations.

depth. Profile B (eastern 50 km of segment 2 described in Section 2.2 of the article) constitutes a transitional segment, which hosts moderate magnitude earthquakes (Figure 2), and has a shallower locking depth compared to profile A (see Section S4 in the supplementary materials of this article). Profile C captures the 45 km long creeping segment (segment 3) of the EPF.

4.3. STTF, CRF, and SCF

Interseismic behavior was next modeled for the major faults accommodating CA-SA relative plate motion in the vicinity of Trinidad and Tobago; the STTF, CRF, and SCF. The analysis was carried out using both GPS velocities and velocities from InSAR time series analysis. First, we inverted GPS-derived horizontal velocities for interseismic slip deficit and locking depth on the three known faults, with velocities projected parallel to the strike of the CRF (Figure 6). We used the inter-fault spacing values of Weber et al. (2020) for the STTF (50 km), CRF (0 km), and SCF (−40 km). Due to the lack of nearfield GPS data for the STTF and lack of GPS data south of the SCF, we also inverted for slip rates for a variety of models with fixed locking depths (i.e., 2, 5, 10, and 15 km) for both the STTF and SCF.

Second, we modeled the InSAR line-of-sight (LOS) velocities over an area that covers most of Trinidad and the entire onshore trace of the CRF. We modeled three velocity profiles normal to the CRF (i.e., I1, I2, and I3) (Figure 6), extracted from the SBAS-derived velocity field. InSAR LOS velocities were inverted with the MC scheme, where random sampling was done within ± 5 mm/yr of the LOS velocities. Modeled LOS velocities were then projected to fault-parallel horizontal velocities. The look vector of ALOS-2 is [north = −0.5035, east = −0.0998, vertical = 0.8582] and, assuming the relative motion across the CRF has no vertical component, we recovered the horizontal velocity using the following equation,

$$|\mathbf{CRF}| = \frac{|\mathbf{LS}|}{\mathbf{LS} \cdot \mathbf{CRF}}$$

where \mathbf{LS} is the look vector and \mathbf{CRF} is the vector of the strike of the CRF.

4.4. Geodetic & Seismic Moment Analyses

One of the principal aims of this study was to compare variations in historic seismic moment release and current interseismic strain accumulation along the plate boundary. To do this, for each segment of the plate boundary we estimated the geometric moment deficit from our modeled slip rates and locking depths using the following relationship:

$$M = G\Delta wDL$$

where G is the crustal shear modulus, which was assumed to be 30 GPa (e.g., Smith-Konter et al., 2011), Δw (m) is the magnitude of the slip deficit for a given period of time, L (m) is the fault length, and D (m) is the inversion-derived locking depth.

To determine the seismic moment released along the plate boundary, we use location-magnitude data from the ISC catalog (Storchak et al., 2015, 2017). We find this catalog to be complete from 1970 to 2017 for earthquake magnitudes 3.5 to 7 and for shallow (<20 km) depths. The catalog was first declustered (Reasenber, 1985) to remove the numerous triggered earthquakes and aftershocks (45% of complete catalog) that are associated with deep intra-slab or STEP-related earthquakes (i.e., Paria Cluster earthquakes; see Govers & Wortel, 2005; Russo & Speed, 1992), whose low-accuracy hypolocation depths were less than or equal to 20 km. We then converted reported non-moment magnitudes (e.g., M_i or m_b) to moment magnitude (M_w) following Gutenberg and Richter (1956), Katsuyuki (1981), and Scordilis (2006). Finally, using our revised magnitude-uniform catalog, and following Kanamori (1977), the total seismic moment released between 1970 and 2017 was calculated for the main fault segments of the plate boundary.

5. Results

Our model results span the entire ~900 km long CA-SA transform plate boundary for the first time, highlighting the variable nature and complexity of strain accumulation and partitioning along the full length of this transform boundary. We summarize the results for each fault system below and in Table 1.

5.1. San Sebastian and La Victoria Faults

Inversion of the GPS velocities from Pérez et al. (2018) yielded slip deficits of 16.4 ± 1.6 mm/yr and 4.3 ± 1.0 mm/yr and locking depths of 7.7 ± 5.2 km and 16.2 ± 4.0 km, for the SSF and LVF, respectively (Figure 7; Table 1). The estimated locking depths have large uncertainties (≥ 4 km) and log-normal distributions (Figure S7.2).

5.2. El Pilar Fault

Profiles A, B, and C (Figure 8 and Table 1) demonstrate a clear transition from locking and elastic strain accumulation to creep along-strike on the El Pilar fault. This provides a significant improvement and refinement as previous studies averaged motion on the five disparate segments into one single “average” profile (e.g., Reinoza et al., 2015). Profile A has a slip deficit of 18.6 ± 1.8 mm/yr and a locking depth of 6.7 ± 2.2 km. Traversing eastward, at longitude $\sim 64^\circ$ W, the locking depth decreases sharply to 1 km in Profile B where this segment creeps at a rate of 17.6 ± 1.0 mm/yr. An equivalent slip rate of 15.8 ± 3.6 mm/yr and a locking depth of 1.0 ± 2.0 km was obtained for profile C, which indicates that the entire 200 km long eastern segment (segments 2, 3, and 4 and east of 64° W) of the EPF was creeping during the observation period.

Table 1
Model Results

	This study		Other studies	
	<i>D</i> (km)	<i>V_{FF}</i> (mm/yr)	<i>D</i> (km)	<i>V_{FF}</i> (mm/yr)
SSF	7.7 ± 5.1	16.4 ± 1.6	14 ± 3 ^a	17.0 ± 0.5 ^a
LVF	16.2 ± 4.0	4.3 ± 1.0	14 ± 3 ^a	2.6 ± 0.4 ^a
EPF			1.6 ^b	20 ^b
Profile A	6.7 ± 2.2	18.6 ± 1.8		
Profile B	1.0 ± 0.6	17.6 ± 1.0		
Profile C	1.0 ± 2.0	15.8 ± 3.6		
SCF	0.0 ± 0.1	3.1 ± 0.1		
CRF-GPS	0.6 ± 0.1	14.8 ± 0.1	0.2 ± 0.2 ^c	13.4 ± 0.3 ^c
STTF	8.0 ± 0.2	3.0 ± 0.1		
CRF-InSAR				
Profile I1	0.1 ± 0.2	14.5 ± 2.0		
Profile I2	0.2 ± 0.3	15.1 ± 2.0		
Profile I3	0.9 ± 1.5	19.2 ± 2.7		

^aPérez et al. (2018). ^bReinoza et al. (2015). ^cWeber et al. (2020).
Abbreviations: CRF, Central Range fault; EPF, El Pilar fault; GPS, Global Positioning System; LVF, La Victoria fault; SSF, San Sebastian fault; STTF, Sub-Tobago Terrane fault.

5.3. STTF, CRF and SCF

Results from inversion of GPS data for the western CRF and the remaining onshore segment of the CRF using InSAR-derived velocities demonstrate for the first time that the entire onshore CRF in Trinidad is creeping over the examined observation period (Figures 9 and 10). Inversion of the GPS data set for the STTF, CRF, and SCF demonstrates that the CRF accommodates ~14.5 mm/yr or ~70% of relative plate motion (Table 1; Figure 9). The best-fit model (i.e., lowest reduced chi-square; Table S6.1), where the locking depths for all faults were estimated, produced a shallow CRF locking depth (0.5 km), and slip deficit rates

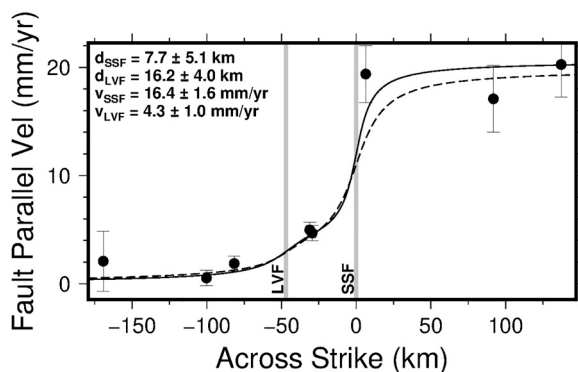


Figure 7. Global Positioning System-derived fault parallel, horizontal velocity profile for the La Victoria (LVF) and San Sebastian (SSF) faults. This study's elastic dislocation model with locking depths of 16.2 ± 4.0 km and 7.7 ± 5.1 km for the LVF and SSF, respectively, and slip distributed on the LVF and SSF at 4.3 ± 1.0 mm/yr and 16.4 ± 1.6 mm/yr, respectively (black line). Dashed line: elastic dislocation model of Pérez et al. (2018) with locking depths on both faults at 14 km, and slip on the LVF and SSF are 2.6 mm/yr and 17 mm/yr, respectively. *d*, locking depth. *v*, relative motion across fault.

for the STTF and SCF of 3.0 ± 0.1 mm/yr each. Of note, the best-fit model produced a locking depth of 8.0 ± 0.2 km for the STTF and 0.0 ± 0.1 km for the SCF. All other models, with locking depths of the STTF and SCF held fixed from 2 to 15 km, produced χ^2 values that were an order of magnitude larger than that of the best-fit model, which is, therefore, our preferred solution. While there is no geodetic data south of the SCF we are confident of the estimated slip rate and locking depth on this fault. Our modeling assumption requires the geodetic signature to be symmetric across the fault and that the fault-parallel velocity tends to zero south of the SCF because of the fixed stable South America reference frame. A maximum locking depth of 3 km is required to fit velocities within 10 km of the SCF.

The InSAR velocity field confirms and expands on the results of Weber et al. (2020), which showed that no additional faults in Trinidad are currently active nor accumulating strain. Inversion results from the InSAR data also confirm that the CRF is creeping: all profiles (I1, I2, and I3) produced extremely shallow locking depths of less than $1 \pm \sim 0.8$ km (Table 1; Figure 10). InSAR profile I1 (Figure 10) produced a creeping rate of 14.5 ± 2.0 mm/yr, in agreement with the GPS model results. Model results for profiles I2 and I3 yielded creeping rates of 15.1 ± 2.0 mm/yr

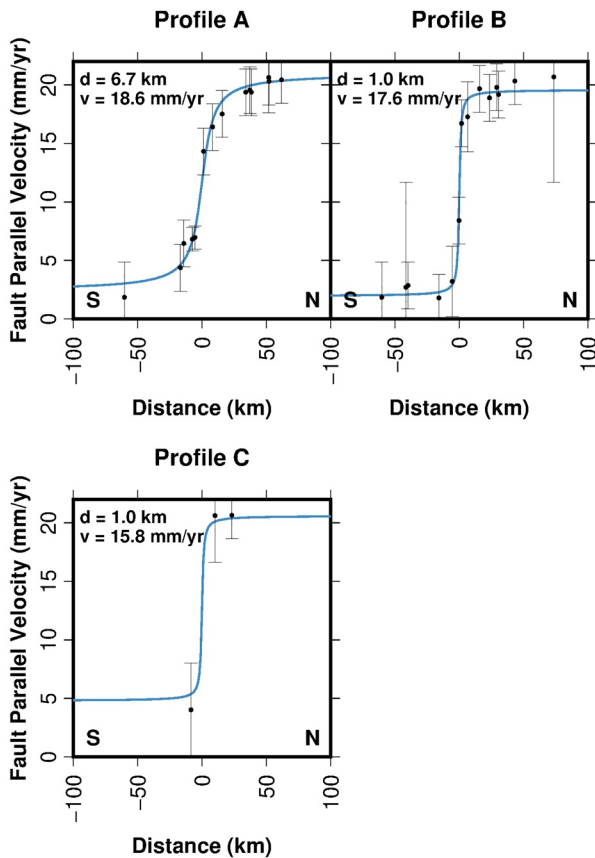


Figure 8. Global Positioning System fault velocity profiles and best-fit elastic dislocation models for El Pilar fault profiles A, B, and C (see Figure 5 for locations). Best-fit model parameters for locking depth (d) and slip deficit (v) are given on each plot.

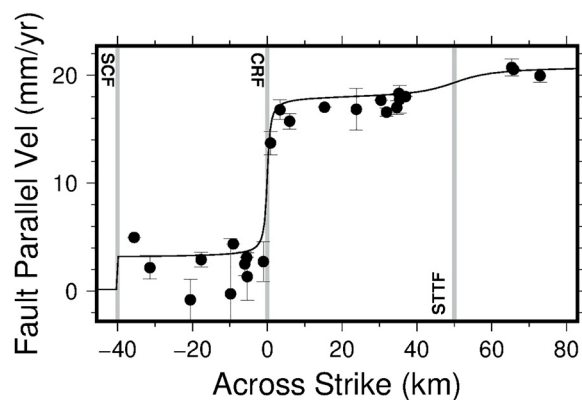


Figure 9. Global Positioning System-derived fault-parallel horizontal velocity profile across the South Coast (SCF), Central Range (CRF) and Sub-Tobago Terrane (STTF) faults, Trinidad-Tobago. Black line is the best fit elastic dislocation model with locking depths on the SCF, CRF, and STTF of 0.0 ± 0.1 km, 0.6 ± 0.1 km, and 8.0 ± 0.2 km, respectively. Best fit model slip rates for the SCF, CRF, and STTF are 3.1 ± 0.1 mm/yr, 14.8 ± 0.1 mm/yr, and 3.0 ± 0.1 mm/yr.

and 19.2 ± 2.7 mm/yr, respectively, which are equivalent to profile 11 within uncertainty.

5.4. Geodetic & Seismic Moment Analyses

Analysis of the geodetically derived moment deficit and the total seismic moment released from 1970 to 2017 shows that a key along-strike transition is present in the plate boundary (Figure 11). The transition for both the geodetic moment deficit and the total seismic moment is located at $\sim 64^\circ\text{W}$ longitude. West of this longitude, the total seismic moment is roughly an order of magnitude lower than that in the eastern segments, whereas the geodetic moment deficit is an order of magnitude larger than that of the eastern segments. The STTF is the single exception, where the seismic moment and moment deficit are equivalent (Figure 11).

6. Discussion

Continental transform plate boundaries are complex zones of deformation that typically exhibit significant along-strike variations in interseismic fault behavior and strain partitioning (Harris, 2017, and references therein). These are parameters that in turn correlate with seismogenesis. Prior to our study, no unified study of the entire ~ 900 km long CA-SA transform plate boundary existed. We discovered and documented that systematic and significant transitions in interseismic fault behavior (i.e., locked to creeping), strain partitioning, and moment release exist along the CA-SA transform plate boundary (Figure 11). Here, we discuss our findings and compare the CA-SA plate boundary with other continental transform systems.

6.1. Interseismic Strain Accumulation & Partitioning

We find that faults in the western segment (west of 64°W) of this plate boundary are locked, whereas those in the east (east of 64°W), with one exception (i.e., the STTF), are creeping. In the west, our inversion results show that both the SSF and LVF are locked to seismogenic depths (i.e., ~ 7 and ~ 16 km depth, respectively) (Figures 6 and 7). Our results also indicate that the ~ 21 mm/yr of CA-SA relative plate motion (Kreemer et al., 2014) is partitioned across these two faults, with the SSF accommodating ~ 16 mm/yr and the LVF ~ 4 mm/yr.

Seismic segmentation of the EPF has previously been recognized based on; for example, aftershock locations and observed surface ruptures from the 1997 M_w 6.8 Cariaco earthquake (Audemard, 2007; Baumbach et al., 2004). Our modeling results confirm that the EPF is indeed segmented, with its western and eastern segments exhibiting significantly different interseismic behaviors. The western EPF (i.e., EPF segment 1; profile A in Figure 5) has a locking depth of 6.7 ± 2.2 km (Figure 8), similar to that of the SSF, and a slip deficit of 18.6 ± 1.8 mm/yr. The EPF transitions to shallower locking at segment 2 (i.e., profile B in Figure 5), which continues along the entire eastern segment (i.e., segments 3 and 4; profile C in Figure 5). The locking depth along these segments (2, 3, & 4) is shallow at ~ 1 km (Figure 8; Table 1) and accommodates 17.6 ± 1.0 mm/yr. Because of the shallow locking depth result, we consider the entire eastern segment of the EPF to be creeping at close to the full relative plate rate from $\sim 64^\circ\text{W}$ longitude to the Gulf of Paria pull-apart basin. As noted

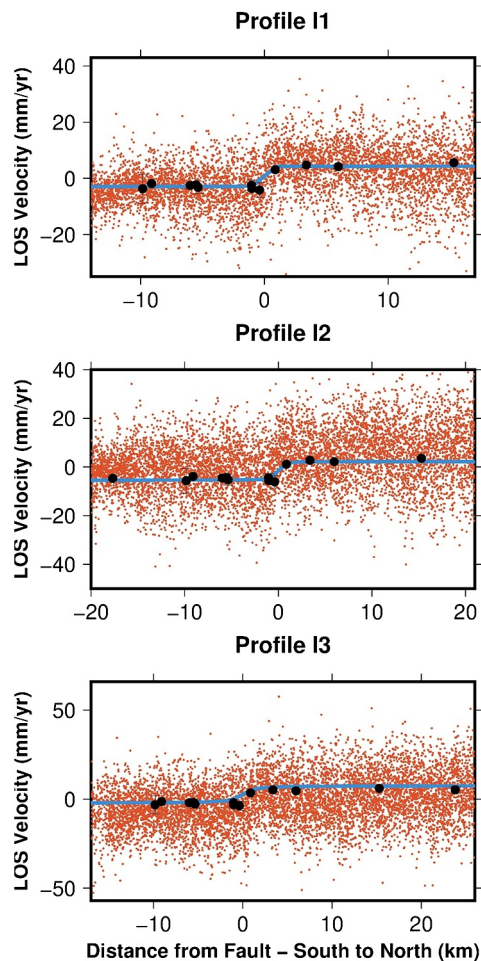


Figure 10. InSAR LOS velocities across the Central Range fault and model fit (blue line) for Profiles I1 (top), I2 (middle), and I3 (bottom). Profile locations are shown in Figure 6. Black circles are Trinidad Global Positioning System velocities projected into LOS for comparison.

in Section 3.1, there is ~ 3 mm/yr residual shear deficit between our model results and the CA-SA relative plate motion rate along the EPF. This residual deficit might be accommodated by shear within the Serrania del Interior, south of the EPF. However, we have insufficient data to place this shear deformation onto any individual structures.

In the easternmost section of the plate boundary (i.e., islands of Trinidad and Tobago) our results indicate variable interseismic behavior and partitioning between three active faults. The STTF is locked to a depth of 8.0 ± 0.2 km and the CRF and SCF are both creeping (i.e., interseismic locking at < 1 km depth). These results are consistent with those of Weber et al. (2020). Our InSAR analysis, however, provides two important new findings: (a) the CRF has a visually identifiable consistent strike of $\sim 70^\circ$ (i.e., aligned parallel with CA-SA plate motion) across all of Trinidad (Figure 6; Table S5.1), and (b) the CRF is creeping along its entire onshore length. The former is an important result, as the eastern CRF trace has proven difficult to map (see e.g., Crosby et al., 2009). The latter result is important as paleoseismic studies have shown that the western segment of the CRF ruptured between 2710 year BP and 550 year BP (Prentice et al., 2010), suggesting the possibility of both temporally and/or spatially variable interseismic strain accumulation. Our results indicate that interseismic strain is partitioned across these three main faults, with 3.1 mm/yr on the STTF, ~ 14.5 mm/yr on the CRF, and 3.0 mm/yr on the SCF, in general agreement with the results of Weber et al. (2020). There are several well-studied analogs to the CA-SA transform plate boundary that also display along-strike variations in interseismic behavior and strain partitioning. Geodetic studies of the North Anatolian fault zone have revealed locked and creeping segments with clear transition zones (Cetin et al., 2014). The San Andreas fault (SAF) also demonstrates locked and creeping segmentation, along with variable seismic moment release rates along its various segments (Smith-Konter et al., 2011), and strain partitioning at its ends. Various proportions of creep occur between the locked NW and SE segments of the SAF, which produced the 1906 and 1857 ruptures, respectively (Wallace, 1970). The Parkfield segment is a ~ 40 km-long transitional segment at the SE end of the 140 km long creeping segment of the SAF (Bakun et al., 2005; Murray et al., 2001; Titus et al., 2006). Finally, $\sim 75\%$ of PA-NA plate motion is accommodated

on three transform faults systems in the north, the single San Andreas fault in the central segment, and then up to five transform faults in the south (Lisowski et al., 1991), analogous to the two-fault (SSF and LVF) one-fault (EPF) three-fault (STTF, CRF, and SCF) system of the CA-SA transform plate boundary described here.

6.2. Geodetic and Seismic Moment

Our modeling results and analyses indicate a spatial correlation between interseismic behavior and seismic moment release along the CA-SA plate boundary. Figure 11 (B & C) shows the geodetically derived moment deficit and the total seismic moment for the plate boundary from 1970 to 2017 for shallow (< 20 km) and $M > 3.5$ earthquakes. Our earthquake data analysis shows that the seismic moment release rates are significantly higher on the eastern (creeping) segment than on the western (locked) segment of the plate boundary. The transition from locked to creeping (profile B) correlates well with the change in the pattern of moderate magnitude seismicity (Figure 2), and therefore the seismic moment release (Figure 11b), and occurs over a ~ 20 km wide segment of the EPF (see Section S4). There is a large and significant deficit in seismic moment release ($\sim 10^{20}$ Nm) along the western plate boundary segment, with interseismic strain accumulating on the SSF, LVF, and western EPF at close to the full plate motion rate. This is expected as these segments are currently locked and accumulating interseismic strain. Moderate to large earthquakes are

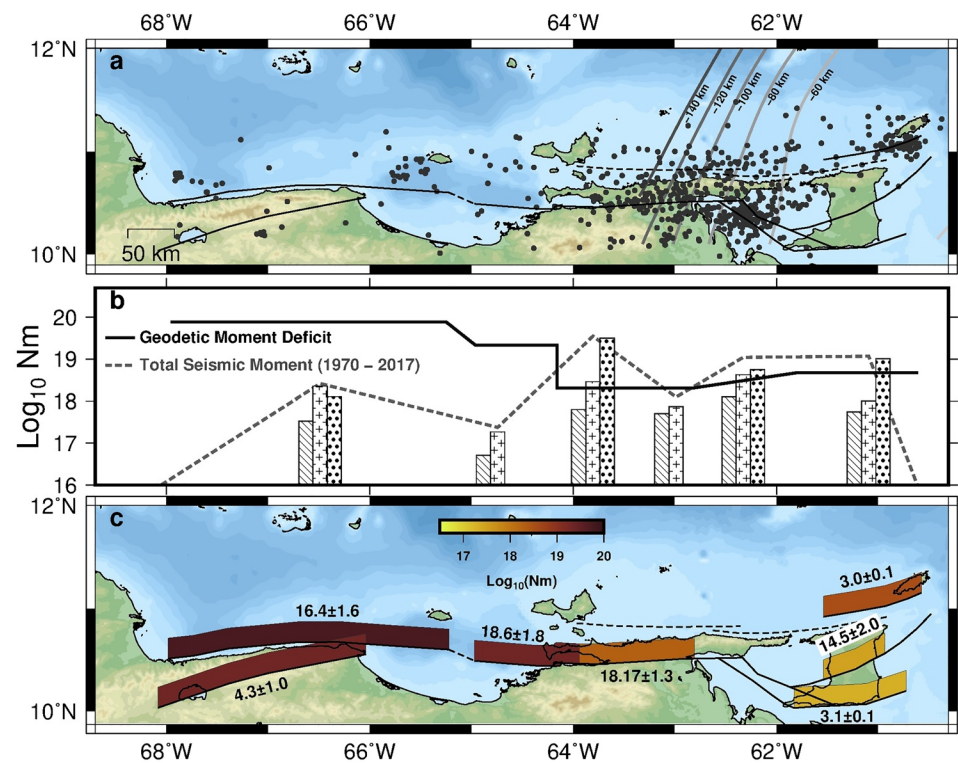


Figure 11. (a) Shallow earthquakes (<20 km) and magnitudes greater than M4 from the ISC catalog (1970–2017). Gray-scale lines show the depth of the subducted SA slab (Hayes et al., 2018). (b) Total seismic moment released (dashed line) along the plate boundary from 1970 to 2017, including total moment contributions for magnitude bins M4 to M5 (diagonal striped bar), M5 to M6 (cross hatched bar), and M6 to M7 (circle hatched bar). Estimated accumulated geodetic moment deficit (solid black line) from inversion-derived locking depths and slip deficits for each segment for the same period (1970–2017, 47 years), which was calculated, per segment, with a shear modulus of 30 GPa, the inversion derived slip deficit, the period of the complete ISC catalog (47 years), and fault area from the segment's length and inversion derived locking depths. For creeping segments, a nominal value of 500 m was used as the locking depth. (c) The calculated accumulated geodetic moment deficit along the plate boundary, except for the STTF (20 years, 1997 to 2017) taking into account the Mw 6.7 1997 Tobago earthquake. Estimated slip deficits and creeping rates (mm/yr) for each fault are provided.

known to have occurred on the SSF, LVF, and western EPF with the largest historical event being the 1900 M 7.6 to M 8.0 on the eastern segment of the SSF (Colón et al., 2015; Pérez, 1998a; Pérez et al., 1997, 2018). There has not been a large magnitude ($M \geq 6.5$) earthquake on the western segment of the EPF since 1929. The largest instrumentally observed earthquake on the LVF was the May 4, 2009 M_w 5.4 (Storchak et al., 2015). Previous to this event were the $M \geq 6.5$ earthquakes in 1641 and 1878. These earthquakes suggest that moderate magnitude earthquakes on the LVF have a reoccurrence interval between ~ 130 and ~ 200 years. Our estimated slip deficit and locking depth for the LVF requires a future M_w 5.5 earthquake with a repeat time of 200 years.

If we assume that the SSF and western EPF could behave as one single fault (total length of ~ 400 km) and that an earthquake with a repeat time of 100 years nucleates at the estimated locking depth of ~ 7 km for the SSF and EPF, then it is possible to produce another $M_w \sim 8.0$ earthquake, similar to that which occurred in 1900. One M_w 8.0 earthquake on the western segment of the plate boundary would recover the moment deficit we find for this region (Figure 11). While continental strike-slip faults rarely produce such large magnitude earthquakes (Harris, 2017), we posit that this scenario could be quite possible. Analogous earthquakes include the 1872 M_w 7.8–7.9 Owen's Valley, California (Hough & Hutton, 2008), and the 2002 M_w 7.9 Denali, Alaska earthquakes (Eberhart-Phillips et al., 2003). A M_w 8.0 is likely the maximum magnitude for an earthquake on the CA-SA transform plate boundary. Considering that earthquakes on continental strike-slip faults do not generally propagate through creeping segments (e.g., Jolivet et al., 2013; Murray &

Langbein, 2006) the rupture strike length for the western CA-SA transform plate boundary is likely limited to that discussed above.

The earthquake catalog we used here (ISC reviewed catalog; Storchak et al., 2015, 2017) is temporally aliased, as it does not include historical earthquakes; for example, the 1929 M_{6.5} Cumana earthquake. However, including historical seismicity for the last 400 years on the SSF and LVF (e.g., M > 6 1641 and 1878 LVF; Pérez, 1998b; and M 7.7 1900 SSF earthquakes; Pacheco & Sykes, 1992), the total seismic moment release is essentially the same for all segments of the plate boundary.

In contrast to the western segment of the CA-SA plate boundary, the central and eastern segments of the EPF have a much higher frequency of low to moderate magnitude earthquakes (Figures 2 and 11). The central EPF (segment 2; profile B), a transition zone between the locked western EPF and the creeping eastern segment, has produced at least two M_w 6–M_w 7 earthquakes in the last 50 years (Figure 2). The 100 km long eastern segment of the EPF accommodates ~95% of the seismic moment via creep and low magnitude earthquakes ($M \leq 5$) (Figure 11). This is similar to the creeping segment of the SAF northwest of Parkfield, along which aseismic creep takes up a significant part of its slip budget, while still producing moderate magnitude earthquakes; for example, the 2004 M_w 6.0 Parkfield earthquake (Bakun et al., 2005; Gans et al., 2003; WGCEP, 2003). The SCF and CRF creep aseismically while the STTF is locked and is seismically active, having ruptured during the 1997 M_w 6.7 earthquake. A similar magnitude earthquake on the STTF will have a reoccurrence interval of ~200 years.

6.3. Correlation Between Interseismic Behavior and Geology

Geodetic studies of continental transform faults have stimulated studies that correlate interseismic fault behavior (i.e., locked to creeping) with the geology of the fault zones, in particular emphasizing possible geologic causes for fault creep. Cetin et al. (2014) determined that creep on the North Anatolian fault is spatially associated with serpentinite and carbonate bedrock lithologies. The creeping segment of the Longitudinal Valley Fault, Taiwan is associated with the Lichi mélange, whereas the locked segment cuts through more competent forearc sedimentary and volcanoclastic units (Thomas et al., 2014). Thomas et al. (2014) suggest that the composition of the mélange helps to facilitate pressure-solution creep, which in turn allows for aseismic slip and creep. The Parkfield segment of the SAF is thought to creep due to the presence of talc-lubricated fault gouge (Moore & Rymer, 2007). In this section, we explore whether the interseismic behavior and seismogenic nature of the faults in the CA-SA transform plate boundary could be a function of geology.

The western segment of the plate boundary defined by the active SSF, LVF, and western EPF cut predominantly high-grade (blueschist-bearing) metamorphic rocks in the coastal mountains (Caracas-Araya-Margarita belt), and further inboard cut ophiolite-bearing rocks of the Cauagua-El Tinaco and Paracotos belt (Figure 3). The central plate boundary segment of the EPF separates low-grade metamorphic rocks of the coastal Paria-Northern Range belt from the sedimentary cover rocks of the passive margin and foreland. According to our modeling results, the transition from western EPF locking to eastern EPF creep occurs at ~64°W. While CRF creep has been suggested to be due to elevated pore fluid pressures related to thermogenic oil and gas and mud volcanoes on the south side of the CRF (Weber et al., 2020), that same mechanism cannot be inferred for creep on the eastern EPF. The oil fields of eastern Venezuela are ~100 km south of the EPF (French & Schenk, 2004). Eastern EPF creep might therefore be due to the geology observed across the fault and/or in the subsurface. On the north side of the ~64°W transition, rocks in the coastal mountains change from Paria-Northern Range to Caracas-Araya-Margarita metamorphics. In addition, gypsum, which is known to be a weak mineral phase, occurs in the Cariaquito/Laventille unit along the southern flanks of the Paria-Northern Range belt (Cruz et al., 2007). Old (Cretaceous) and topographically high passive margin sedimentary rocks south of the eastern EPF transition to younger (Paleogene-Neogene) and topographically lower foreland basin fill to the southwest. The subsurface position of the Jurassic Espino graben is also somewhat coincident with the observed ~64°W transition. The geology may therefore play a role in creep on the eastern EPF, but more detailed investigations are still needed.

7. Conclusions

The ~900 km long CA-SA transform plate boundary from 68°W to 60°W is characterized by significant along-strike strain partitioning and variability in interseismic behavior. We find that the plate boundary faults west of 64°W are locked, while faults east of this longitude, except for one (STTF), are creeping. Despite displaying predominantly active creep, many of the faults in the eastern plate boundary are currently or have been seismogenic. These spatial and temporal variations in seismic moment release are most likely governed by geology and/or changes in pore fluid pressures. We find that the CRF is the only active fault on the island of Trinidad; it is creeping along its entire ~50 km length, and it accommodates 70% of the CA-SA relative motion. The remaining 30% of plate motion at this longitude is partitioned onto the STTF and SCF. Future work, including establishing borehole seismometers, strain and creepmeters, and a denser cGPS network, is needed to better characterize time-varying strain and the seismogenic potential of the CRF. Further work is needed to determine the mechanism that allows for creep on the eastern EPF. Our findings lead us to infer that the entire western segment of the CA-SA transform plate boundary may be capable of rupturing a M_w 8 earthquake, an inference that should help guide future seismic hazard and risk zonation for this populated region.

Data Availability Statement

ALOS-2 SAR data were made available by the Japanese Aerospace Exploration Agency (JAXA) for the sixth RA proposal (PI no. 3153). The data used in this paper can be accessed at <https://doi.org/10.26207/kh1e-z633>.

Acknowledgments

The authors wish to acknowledge all of those who have collected and published GPS-GNSS data in the region. We thank two anonymous reviewers for their constructive comments and the editorial oversight of Taylor Schildgen.

References

- Amante, C., & Eakins, B. W. (2009). *ETOPO1 1 arc-minute global relief model: Procedures, data sources and analysis*.
- Audemard, F. A. (2006). Surface rupture of the Cariaco July 09, 1997 earthquake on the El Pilar fault, northeastern Venezuela. *Tectonophysics*, 424(1–2), 19–39. <https://doi.org/10.1016/j.tecto.2006.04.018>
- Audemard, F. A. (2007). Revised seismic history of the El Pilar fault, Northeastern Venezuela, from the Cariaco 1997 earthquake and recent preliminary paleoseismic results. *Journal of Seismology*, 11(3), 311–326. <https://doi.org/10.1007/s10950-007-9054-2>
- Avé Lallemant, H. G. (1997). Transpression, displacement partitioning, and exhumation in the eastern Caribbean/South American plate boundary zone. *Tectonics*, 16(2), 272–289. <https://doi.org/10.1029/96TC03725>
- Avé Lallemant, H. G., & Sisson, V. B. (2005). Exhumation of eclogites and blueschists in northern Venezuela: Constraints from kinematic analysis of deformation structures. *Geological Society of America Special Paper*, 394, 193–206. [https://doi.org/10.1130/2005.2394\(07](https://doi.org/10.1130/2005.2394(07)
- Bakun, W. H., Aagaard, B., Dost, B., Ellsworth, W. L., Hardebeck, J. L., Harris, R. A., et al. (2005). Implications for prediction and hazard assessment from the 2004 Parkfield earthquake. *Nature*, 437(7061), 969–974. <https://doi.org/10.1038/nature04067>
- Baumbach, M., Grosser, H., Torres, G., Rojas Gonzales, J. L., Sobiesiak, M., & Welle, W. (2004). Aftershock pattern of the July 9, 1997 $M_w = 6.9$ Cariaco earthquake in Northeastern Venezuela. *Tectonophysics*, 379(1–4), 1–23. <https://doi.org/10.1016/j.tecto.2003.10.018>
- Beltran, C., Singer, A., & Rodriguez, A. (1996). The El Pilar fault active trace (Northeastern Venezuela): Neotectonic evidences and paleoseismic data. In *Third International Symposium on Andean Geodynamics* (pp. 153–156).
- Beltran, P. L., Pathier, E., François, J., Vassallo, R., Reinoza, C., Audemard, F., et al. (2016). Spatial and temporal variations in creep rate along the El Pilar fault at the Caribbean-South American plate boundary (Venezuela), from InSAR. *Journal of Geophysical Research: Solid Earth*, 121, 8276–8296. <https://doi.org/10.1002/2016JB013121>
- Berardino, P., Fornaro, G., Lanari, R., & Sansosti, E. (2002). A new algorithm for surface deformation monitoring based on small baseline differential SAR interferograms. *IEEE Transactions on Geoscience and Remote Sensing*, 40(11), 2375–2383. <https://doi.org/10.1109/TGRS.2002.803792>
- Billham, R., Ozener, H., Mencin, D., Dogru, A., Ergintav, S., Cakir, Z., et al. (2016). Surface creep on the North Anatolian Fault at Ismetpaşa, Turkey, Turkey, 1944–2016. *Journal of Geophysical Research: Solid Earth*, 121(10), 7409–7431. <https://doi.org/10.1002/2016JB012928>
- Bohnhoff, M., Grosser, H., & Dresen, G. (2006). Strain partitioning and stress rotation at the North Anatolian fault zone from after-shock focal mechanisms of the 1999 Izmit $M_w = 7.4$ earthquake. *Geophysical Journal International*, 166(1), 373–385. <https://doi.org/10.1111/j.1365-246X.2006.03027.x>
- Bos, M. S., Fernandes, R. M. S., Williams, S. D. P., & Bastos, L. (2013). Fast error analysis of continuous GNSS observations with missing data. *Journal of Geodesy*, 87(4), 351–360. <https://doi.org/10.1007/s00190-012-0605-0>
- Boschman, L. M., van Hinsbergen, D. J. J., Torsvik, T. H., Spakman, W., & Pindell, J. L. (2014). Kinematic reconstruction of the Caribbean region since the early Jurassic. *Earth-Science Reviews*, 138, 102–136. <https://doi.org/10.1016/j.earscirev.2014.08.007>
- Burke, K. (1988). Tectonic evolution of the Caribbean. *Annual Review of Earth and Planetary Sciences*, 16(1), 201–230.
- Cavalié, O., Lasserre, C., Doin, M. P., Peltzer, G., Sun, J., Xu, X., & Shen, Z. K. (2008). Measurement of interseismic strain across the Haiyuan fault (Gansu, China), by InSAR. *Earth and Planetary Science Letters*, 275(3–4), 246–257. <https://doi.org/10.1016/j.epsl.2008.07.057>
- Cetin, E., Cakir, Z., Meghraoui, M., Ergintav, S., & Akoglu, A. M. (2014). Extent and distribution of aseismic slip on the Ismetpaşa segment of the North Anatolian Fault (Turkey) from Persistent Scatterer InSAR. *Geochemistry, Geophysics, Geosystems*, 15(7), 2883–2894. <https://doi.org/10.1002/2014GC005307>. Received
- Chen, C. W., & Zebker, H. A. (2000). Network approaches to two-dimensional phase unwrapping: Intractability and two new algorithms. *Journal of the Optical Society of America. A, Optics, Image Science, and Vision*, 17(3), 401–414. Retrieved from <http://www.ncbi.nlm.nih.gov/pubmed/10708020>

- Chen, C. W., & Zebker, H. A. (2002). Phase unwrapping for large SAR interferograms: Statistical segmentation and generalized network models. *IEEE Transactions on Geoscience and Remote Sensing*, 40(8), 1709–1719. <https://doi.org/10.1109/TGRS.2002.802453>
- Colón, S., Audemard, F. A., Beck, C., Avila, J., Padrón, C., De Batist, M., et al. (2015). The 1900 Mw 7.6 earthquake offshore north-central Venezuela: Is La Tortuga or San Sebastián the source fault? *Marine and Petroleum Geology*, 67, 498–511. <https://doi.org/10.1016/j.marpetgeo.2015.06.005>
- Crosby, C. J., Prentice, C. S., Weber, J., & Ragona, D. (2009). *Logs of paleoseismic excavations across the Central Range fault*. Trinidad.
- Cruz, L., Fayon, A. K., Teyssier, C., & Weber, J. (2007). Exhumation and deformation processes in transpressional orogens: The Venezuelan Paria Peninsula, SE Caribbean-South American plate boundary. *Geological Society of America Special Paper*, 434(08), 149–165. [https://doi.org/10.1130/2007.2434\(08\)](https://doi.org/10.1130/2007.2434(08))
- DeMets, C., Gordon, R. G., & Argus, D. F. (2010). Geologically current plate motions. *Geophysical Journal International*, 181(1), 1–80. <https://doi.org/10.1111/j.1365-246X.2009.04491.x>
- Deville, E., & Guerlais, S. H. (2009). Cyclic activity of mud volcanoes: Evidences from Trinidad (SE Caribbean). *Marine and Petroleum Geology*, 26(9), 1681–1691. <https://doi.org/10.1016/j.marpetgeo.2009.03.002>
- Dziewonski, A. M., Chou, T. A., & Woodhouse, J. H. (1981). Determination of earthquake source parameters from waveform data for studies of global and regional seismicity. *Journal of Geophysical Research*, 86(B4), 2825–2852.
- Eberhart-Phillips, D., Haeussler, P. J., Freymueller, J. T., Frankel, A. D., Rubin, C. M., Craw, P., et al. (2003). The 2002 Denali fault earthquake, Alaska: A large magnitude, slip-partitioned event. *Science*, 300(5622), 1113–1118. <https://doi.org/10.1126/science.1082703>
- Ekström, G., Nettles, M., & Dziewonski, A. M. (2012). The global CMT project 2004–2010: Centroid-moment tensors for 13,017 earthquakes. *Physics of the Earth and Planetary Interiors*, 200–201, 1–9. <https://doi.org/10.1016/j.pepi.2012.04.002>
- Engdahl, E. R., Storchak, D. A., Di Giacomo, D., Bondár, I., Harris, J., Lee, W. H. K., et al. (2013). Public release of the ISC—GEM global instrumental earthquake catalogue (1900–2009). *Seismological Research Letters*, 84(5), 810–815.
- Erllich, R., & Barrett, S. F. (1990). Cenozoic Plate tectonic history of the northern Venezuela-Trinidad Area. *Tectonics*, 9(1), 161–184.
- Escalona, A., Mann, P., & Jaimes Martha, M. (2011). Miocene to recent Cariaco basin, offshore Venezuela: Structure, tectonosequences, and basin-forming mechanisms. *Marine and Petroleum Geology*, 28(1), 177–199. <https://doi.org/10.1016/j.marpetgeo.2009.04.001>
- Flinch, J. F., Rambaran, V., Ali, W., Lisa, V. D., Hernandez, G., Rodríguez, K., & Sams, R. (1999). Chapter 17 Structure of the Gulf of paria pull-apart basin (Eastern Venezuela-Trinidad). *Sedimentary Basins of the World*, 4(C), 477–494. [https://doi.org/10.1016/S1874-5997\(99\)80051-3](https://doi.org/10.1016/S1874-5997(99)80051-3)
- French, C. D., & Schenk, C. J. (2004). *Map showing geology, oil and gas fields, and geologic provinces of the Caribbean region*.
- Gans, C. R., Furlong, K. P., & Malservisi, R. (2003). Fault creep and microseismicity on the Hayward fault, California: Implications for asperity size. *Geophysical Research Letters*, 30(19), 8–11. <https://doi.org/10.1029/2003GL017904>
- García-Abdeslem, J., Regalado-Sosa, J. J., & Cerquone-Ravelo, H. R. (2013). Un modelo 3D de la densidad del subsuelo en el graben de Espino: Un aulacógeno Jurásico en el oriente de Venezuela. *Revista Mexicana de Ciencias Geológicas*, 30(1), 110–120.
- Garcíacaro, E., Mann, P., & Escalona, A. (2011). Regional structure and tectonic history of the obliquely colliding Columbus foreland basin, offshore Trinidad and Venezuela. *Marine and Petroleum Geology*, 28(1), 126–148. <https://doi.org/10.1016/j.marpetgeo.2009.08.016>
- Govers, R., & Wortel, M. J. R. (2005). Lithosphere tearing at STEP faults: Response to edges of subduction zones. *Earth and Planetary Science Letters*, 236(1–2), 505–523. <https://doi.org/10.1016/j.epsl.2005.03.022>
- Gutenberg, B., & Richter, C. F. (1956). Earthquake magnitude, intensity, energy, and acceleration: (Second paper). *Bulletin of the Seismological Society of America*, 46(2), 105–145.
- Harris, R. A. (2017). Large earthquakes and creeping faults. *Reviews of Geophysics*, 55(1), 169–198. <https://doi.org/10.1002/2016RG000539>
- Hayes, G. P., Moore, G. L., Portner, D. E., Hearne, M., Flamme, H., Furtney, M., & Smoczyk, G. M. (2018). Slab2, a comprehensive subduction zone geometry model. *Science*, 61(October), 58–61.
- Henry, M., Pentilla, M., & Hoyer, D. (2010). Observations from exploration drilling in an active mud volcano in the southern basin of Trinidad, West Indies. In L. Wood (Ed.), *Shale tectonics* (pp. 63–78). American Association of Petroleum Geologists Memoir. AAPG Special Volumes.
- Heppard, P. D., Cander, H. S., & Eggertson, E. B. (1998). Abnormal pressure and the occurrence of hydrocarbons in offshore eastern Trinidad, West Indies. *AAPG Memoir*, 1902(70), 215–246.
- Higgins, G. E., & Saunders, J. B. (1967). Report on 1964 Chatham Mud Island, Erin Bay, Trinidad, West Indies. *AAPG Bulletin*, 51(1), 55.
- Hough, S. E., & Hutton, K. (2008). Revisiting the 1872 Owens Valley, California, Earthquake. *Bulletin of the Seismological Society of America*, 98(2), 931–949. <https://doi.org/10.1785/0120070186>
- Jolivet, R., Lasserre, C., Doin, M. P., Guillaso, S., Peltzer, G., Dailu, R., et al. (2012). Shallow creep on the Haiyuan fault (Gansu, China) revealed by SAR interferometry. *Journal of Geophysical Research: Solid Earth*, 117(6), 1–18. <https://doi.org/10.1029/2011JB008732>
- Jolivet, R., Lasserre, C., Doin, M. P., Peltzer, G., Avouac, J. P., Sun, J., & Dailu, R. (2013). Spatio-temporal evolution of aseismic slip along the Haiyuan fault, China: Implications for fault frictional properties. *Earth and Planetary Science Letters*, 377, 23–33.
- Jordan, T. H. (1975). The present-day motions of the Caribbean Plate. *Journal of Geophysical Research*, 80(32), 4433–4439. <https://doi.org/10.1029/JB080i032p04433>
- Jouanne, F., Audemard, F. A., Beck, C., Van Welden, A., Ollarves, R., & Reinoza, C. (2011). Present-day deformation along the El Pilar Fault in eastern Venezuela: Evidence of creep along a major transform boundary. *Journal of Geodynamics*, 51(5), 398–410. <https://doi.org/10.1016/j.jjog.2010.11.003>
- Kanamori, H. (1977). The energy release in great earthquakes. *Journal of Geophysical Research*, 82(20), 2981–2987.
- Katsuyuki, A. (1981). Magnitudes of large shallow earthquakes from 1904 to 1980. *Physics of the Earth and Planetary Interiors*, 27(1), 72–92.
- Kreemer, C., Klein, E., Shen, Z. K., Wang, M., Estey, L., Wier, S., & Boler, F. (2014). A geodetic plate motion and Global Strain Rate Model. *Geochemistry, Geophysics, Geosystems*, 130. <https://doi.org/10.1002/2014GC005407>. Received
- Lentas, K. (2017). Towards routine determination of focal mechanisms obtained from first motion P-wave arrivals. *Geophysical Journal International*, 212(3), 1665–1686.
- Lentas, K., Di Giacomo, D., Harris, J., & Storchak, D. A. (2019). The ISC Bulletin as a comprehensive source of earthquake source mechanisms. *Earth System Science Data*, 11(2), 565–578.
- Lidz, L., Ball, M., & Charm, W. (1968). Geophysical measurements bearing on the problem of the El Pilar Fault in the Northern Venezuelan Offshore. *Bulletin of Marine Science*, 18(3), 545–560. Retrieved from <http://www.ingentaconnect.com/content/umrsmas/bullmar/1968/00000018/00000003/art00001>
- Lisowski, M., Savage, J. C., & Prescott, W. H. (1991). The velocity field along the San Andreas fault in central and southern California. *Journal of Geophysical Research*, 96(B5), 8369–8389.

- Maresch, W. V. (1974). Plate tectonics origin of the Caribbean mountain system of Northern South America: Discussion and proposal. *Bulletin of the Geological Society of America*, 85(5), 669–682.
- Maurer, J., & Johnson, K. (2014). Fault coupling and potential for earthquakes on the creeping section of the central San Andreas Fault. *Journal of Geophysical Research: Solid Earth*, 119(5), 4414–4428. <https://doi.org/10.1002/2013JB010741>
- Mendoza, C. (2000). Rupture history of the 1997 Cariaco, Venezuela, earthquake from teleseismic P waves. *Geophysical Research Letters*, 27(10), 1555–1558. <https://doi.org/10.1029/1999GL011278>
- Mocquet, A., Beltran, C., Lugo, M., Rodriguez, J. A., & Singer, A. (1996). Seismological interpretation of the historical data related to the 1929 Cumana Earthquake, Venezuela. In *Third International Symposium on Andean Geodynamics, Saint Malo (France)* (pp. 203–206).
- Molnar, P., & Sykes, L. R. (1969). Tectonics of the Caribbean and Middle America regions from focal mechanisms and seismicity. *The Geological Society of America Bulletin*, 80(September), 1639–1684. [https://doi.org/10.1130/0016-7606\(1969\)80](https://doi.org/10.1130/0016-7606(1969)80)
- Moore, D. E., & Rymer, M. J. (2007). Talc-bearing serpentinite and the creeping section of the San Andreas Fault. *Nature*, 448(7155), 795–797. <https://doi.org/10.1038/nature06064>
- Murray, J. R., & Langbein, J. (2006). Slip on the San Andreas Fault at Parkfield, California, over two earthquake cycles, and the implications for seismic hazard. *Bulletin of the Seismological Society of America*, 96(4 B), 283–303. <https://doi.org/10.1785/0120050820>
- Murray, J. R., Segall, P., Cervelli, P., Prescott, W., & Svarc, J. (2001). Inversion of GPS data for spatially variable slip-rate on the San Andreas Fault near Parkfield, CA. *Geophysical Research Letters*, 28(2), 359–362. <https://doi.org/10.1029/2000GL011933>
- Ostos, M., & Sisson, V. B. (2005). Geochemistry and tectonic setting of igneous and metigneous rocks of northern Venezuela. *Caribbean-South American Plate Interactions, Venezuela*, 394(04), 119–155. <https://doi.org/10.1130/0-8137-2394-9.119>
- Pacheco, J. F., & Sykes, L. R. (1992). Seismic moment catalog of large shallow earthquakes, 1900 to 1989. *Bulletin of the Seismological Society of America*, 82(3), 1306–1349.
- Pérez, O. J. (1998a). Seismological report on the Mw = 6.8 strong shock of 9 July 1997 in Cariaco, Northeastern Venezuela. *Bulletin of the Seismological Society of America*, 88(3), 874–879.
- Pérez, O. J. (1998b). Sismicidad y tectónica en Venezuela y áreas vecinas. *Física de La Tierra*, 1998(10), 87–110.
- Pérez, O. J., Bilham, R., Bendick, R., Velandia, J. R., Hernández, N., Moncayo, C., et al. (2001). Velocity field across the southern Caribbean plate boundary and estimates of Caribbean/South-American plate motion using GPS geodesy 1994–2000. *Geophysical Research Letters*, 28(15), 2987–2990. <https://doi.org/10.1029/2001GL013183>
- Pérez, O. J., Sanz, C., & Lagos, G. (1997). Microseismicity, tectonics and seismic potential in southern Caribbean and northern Venezuela. *Journal of Seismology*, 1(1), 15–28. Retrieved from <http://www.scopus.com/inward/record.url?eid=2-s2.0-0346435794&partnerID=40&md5=f848c9cfc83cd775c9a97f2796032a0>
- Pérez, O. J., Wesnousky, S. G., De La Rosa, R., Márquez, J., Uzcátegui, R., Quintero, C., et al. (2018). On the interaction of the North Andes plate with the Caribbean and South American plates in northwestern South America from GPS geodesy and seismic data. *Geophysical Journal International*, 214(3), 1986–2001. <https://doi.org/10.1093/GJI/GGY230>
- Pindell, J. L., & Barrett, S. F. (1990). *Geological evolution of the Caribbean region; A Plate tectonic perspective* (pp. 405–432). The Geology of North America.
- Pindell, J. L., & Kennan, L. (2001). Processes and events in the terrane assembly of Trinidad and Eastern Venezuela. *Petroleum Systems of Deep-Water Basins: Global and Gulf of Mexico Experience*, 21, 159–192. <https://doi.org/10.5724/gcs.01.21.0129>
- Prentice, C. S., Weber, J. C., Crosby, C. J., & Ragona, D. (2010). Prehistoric earthquakes on the Caribbean-South American plate boundary, central range fault, Trinidad. *Geology*, 38(8), 675–678. <https://doi.org/10.1130/G30927.1>
- Reasenber, P. (1985). Second-order moment of central California seismicity, 1969–1982. *Journal of Geophysical Research*, 90(B7), 5479–5495.
- Reinoza, C., Jouanne, F., Audemard, F. A., Schmitz, M., & Beck, C. (2015). Geodetic exploration of strain along the El Pilar Fault in north-eastern Venezuela. *Journal of Geophysical Research: Solid Earth*, 120(3), 1993–2013. <https://doi.org/10.1002/2014JB011483>
- Robertson, P., & Burke, K. (1989). Evolution of southern Caribbean Plate boundary, vicinity of Trinidad and Tobago. *AAPG Bulletin*, 73(4), 490–509.
- Russo, R. M., & Speed, R. C. (1992). Oblique collision and tectonic wedging of the South American continent and Caribbean terranes. *Geology*, 20(5), 447–450.
- Russo, R. M., & Speed, R. C. (1994). Spectral analysis of gravity anomalies and the architecture of tectonic wedging, NE Venezuela and Trinidad. *Tectonics*, 13(3), 613–622. <https://doi.org/10.1029/94TC00052>
- Russo, R. M., Speed, R. C., Okal, E. A., Shepherd, J. B., & Rowley, K. C. (1993). Seismicity and tectonics of the southeastern Caribbean. *Journal of Geophysical Research*, 98, 299–319. <https://doi.org/10.1029/93JB00507>
- Sandwell, D. T., Xu, X., Mellors, R., Wei, M., Tong, X., & Wessel, P. (2016). *GMTSAR: An InSAR processing system based on generic mapping tools* (2nd ed.). Retrieved from http://topex.ucsd.edu/gmtsar/tar/GMTSAR_2ND_TEX.pdf
- Savage, J. C., & Burford, R. O. (1973). Geodetic determination of relative plate motion in central California. *Journal of Geophysical Research*, 78(5), 832–845.
- Schmidt, D. A., & Bürgmann, R. (2003). Time-dependent land uplift and subsidence in the Santa Clara valley, California, from a large interferometric synthetic aperture radar data set. *Journal of Geophysical Research*, 108(B9). <https://doi.org/10.1029/2002JB002267>
- Schubert, C. (1979). El Pilar fault zone, northeastern Venezuela: Brief review. *Tectonophysics*, 52(1–4), 447–455.
- Schubert, C. (1981). Are the Venezuelan fault systems part of the southern Caribbean plate boundary? *Geologische Rundschau*, 70(2), 542–551. <https://doi.org/10.1007/BF01822134>
- Schubert, C. (1985). Neotectonic aspects of the southern Caribbean plate boundary. In *First Geological Conference of the Geological Society of Trinidad & Tobago* (pp. 265–268). Geological Society of Trinidad & Tobago.
- Schubert, C., & Krause, F. F. (1984). Móron fault zone, north-central Venezuelan borderland: Identification, definition, and neotectonic character. *Marine Geophysical Researches*, 6(3), 257–273.
- Scordilis, E. M. (2006). Empirical global relations converting MS and mb to moment magnitude. *Journal of Seismology*, 10(2), 225–236. <https://doi.org/10.1007/s10950-006-9012-4>
- Şengör, A. M., Tüysüz, O., İmren, C., Sakiç, M., Eyidoğan, H., Görür, N., et al. (2005). The North Anatolian Fault: A New Look. *Annual Review of Earth and Planetary Sciences*, 33(1), 37–112. <https://doi.org/10.1146/annurev.earth.32.101802.120415>
- Sisson, V. B., Avé Lallemand, H. G., Ostos, M., Blythe, A. E., Snee, L. W., Copeland, P., et al. (2005). Overview of radiometric ages in three allochthonous belts of northern Venezuela: Old ones, new ones, and their impact on regional geology. *Caribbean-South American Plate Interactions, Venezuela*, 394(03), 91–118. <https://doi.org/10.1130/0-8137-2394-9.91>
- Sisson, V. B., Ertan, I. E., & Avé Lallemand, H. G. (1997). High-pressure (~2000 MPa) kyanite- and glaucophane-bearing pelitic schist and eclogite from Cordillera de la Costa belt, Venezuela. *Journal of Petrology*, 38(1), 65–83. <https://doi.org/10.1093/ptro/38.1.65>

- Smith-Konter, B. R., Sandwell, D. T., & Shearer, P. (2011). Locking depths estimated from geodesy and seismology along the San Andreas Fault System: Implications for seismic moment release. *Journal of Geophysical Research*, *116*(6), 1–13. <https://doi.org/10.1029/2010JB008117>
- Sorensen, S. S., Sisson, V. B., & Avé Lallemand, H. G. (2005). Geochemical evidence for possible trench provenance and fluid-rock histories, Cordillera de la Costa eclogite belt, Venezuela. *Geological Society of America Special Paper*, *394*(06), 173–192. <https://doi.org/10.1130/2005.SPE394/06>
- Soto, M. D., Mann, P., Escalona, A., & Wood, L. J. (2007). Late Holocene strike-slip offset of a subsurface channel interpreted from three-dimensional seismic data, eastern offshore Trinidad. *Geology*, *35*(9), 859–862. <https://doi.org/10.1130/G23738A.1>
- Speed, R. C. (1985). Cenozoic collision of the Lesser Antilles Arc and continental South America and the origin of the El Pilar Fault. *Tectonics*, *4*(1), 41–69. <https://doi.org/10.1029/TC004i001p00041>
- Stockhert, B. (1995). Crustal history of Margarita Island (Venezuela) in detail: Constraint on the Caribbean plate-tectonic scenario. *Geology*, *23*(9), 787–790.
- Storchak, D. A., Di Giacomo, D., Engdahl, E. R., Harris, J., Bondár, I., Lee, W. H. K., et al. (2015). The ISC-GEM global instrumental earthquake catalogue (1900–2009): Introduction. *Physics of the Earth and Planetary Interiors*, *239*, 48–63.
- Storchak, D. A., Harris, J., Brown, L., Lieser, K., Shumba, B., Verney, R., et al. (2017). Rebuild of the Bulletin of the International Seismological Centre (ISC), part 1: 1964–1979. *Geoscience Letters*, *4*(1). <https://doi.org/10.1186/s40562-017-0098-z>
- Suárez, G., & Nábělek, J. (1990). The 1967 Caracas earthquake: Fault geometry, direction of rupture propagation and seismotectonic implications. *Journal of Geophysical Research: Solid Earth*, *95*(B11), 17459–17474.
- Symithe, S., Calais, E., De Chabaliér, J. B., Robertson, R., & Higgins, M. (2015). Current block motions and strain accumulation on active faults in the Caribbean. *Journal of Geophysical Research: Solid Earth*, *120*(5). <https://doi.org/10.1002/2014JB011779>
- Thomas, M. Y., Avouac, J. P., Gratier, J. P., & Lee, J. C. (2014). Lithological control on the deformation mechanism and the mode of fault slip on the Longitudinal Valley Fault, Taiwan. *Tectonophysics*, *632*(C), 48–63. <https://doi.org/10.1016/j.tecto.2014.05.038>
- Titus, S. J., DeMets, C., & Tikoff, B. (2006). Thirty-five-year creep rates for the creeping segment of the San Andreas Fault and the effects of the 2004 Parkfield earthquake: Constraints from alignment arrays, continuous global positioning system, and creepmeters. *Bulletin of the Seismological Society of America*, *96*(4 B), 250–268. <https://doi.org/10.1785/0120050811>
- Tong, X., & Schmidt, D. (2016). Active movement of the Cascade landslide complex in Washington from a coherence-based InSAR time series method. *Remote Sensing of Environment*, *186*, 405–415.
- Wallace, R. E. (1970). Earthquake recurrence intervals on the San Andreas fault. *The Geological Society of America Bulletin*, *81*(10), 2875–2890.
- Wang, C., Shan, X., Wang, C., Ding, X., Zhang, G., & Masterlark, T. (2013). Using finite element and Okada models to invert coseismic slip of the 2008 Mw 7.2 Yutian earthquake, China, from InSAR data. *Journal of Seismology*, *17*(2), 347–360. <https://doi.org/10.1007/s10950-012-9324-5>
- Weber, J. C. (2010). Neotectonics in the Trinidad and Tobago, West Indies segment of the Caribbean-South American plate boundary. *Occasional Papers of the Geological Institute of Hungary*, *204*, 21–29.
- Weber, J. C., Dixon, T. H., DeMets, C., Ambeh, W. B., Jansma, P., Mattioli, G., et al. (2001). GPS estimate of relative motion between the Caribbean and South American plates, and geologic implications for Trinidad and Venezuela. *Geology*, *29*(1), 75–78.
- Weber, J. C., Geirsson, H., La Femina, P., Robertson, R., Churches, C., Shaw, K., et al. (2020). Fault creep and strain partitioning in Trinidad-Tobago: Geodetic measurements, models, and origin of creep. *Tectonics*, *39*(1), 1–15. <https://doi.org/10.1029/2019TC005530>
- Weber, J. C., Geirsson, H., Latchman, J. L., Shaw, K., La Femina, P., Wdowinski, S., et al. (2015). Tectonic inversion in the Caribbean-South American plate boundary: GPS geodesy, seismology, and tectonics of the Mw 6.7 22 April 1997 Tobago earthquake. *Tectonics*, *34*(6), 1181–1194. <https://doi.org/10.1002/2014TC003665>. Received
- Weber, J. C., Saleh, J., Balkaransingh, S., Dixon, T., Ambeh, W., Leong, T., et al. (2011). Triangulation-to-GPS and GPS-to-GPS geodesy in Trinidad, West Indies: Neotectonics, seismic risk, and geologic implications. *Marine and Petroleum Geology*, *28*(1), 200–211. <https://doi.org/10.1016/j.marpetgeo.2009.07.010>
- Wei, M., & Sandwell, D. T. (2010). Decorrelation of L-band and C-band interferometry over vegetated areas in California. *IEEE Transactions on Geoscience and Remote Sensing*, *48*(7), 2942–2952. <https://doi.org/10.1109/TGRS.2010.2043442>
- WGCEP. (2003). Earthquake probabilities in the San Francisco Bay region: 2002–2031. *U.S. Geological Survey*, *2003*(214), 1–340.
- Willemann, R. J., & Storchak, D. A. (2001). Data collection at the International Seismological Centre. *Seismological Research Letters*, *72*(4), 440–453. <https://doi.org/10.1785/gssrl.72.4.440>
- Xu, X., Sandwell, D. T., Tymofeyeva, E., González-Ortega, A., & Tong, X. (2017). Tectonic and anthropogenic deformation at the Cerro Prieto geothermal step-over revealed by Sentinel-1A InSAR. *IEEE Transactions on Geoscience and Remote Sensing*, *55*(9), 5284–5292.
- Ysaccis, B. R. (1998). *Tertiary evolution of the northeastern Venezuela offshore*. (Doctoral dissertation). Rice University. Retrieved from <https://scholarship.rice.edu/handle/1911/19330>

References From the Supporting Information

- Altamimi, Z., Métivier, L., & Collilieux, X. (2012). ITRF2008 plate motion model. *Journal of Geophysical Research: Solid Earth*, *117*(7), 1–14. <https://doi.org/10.1029/2011JB008930>
- Bertiger, W., Desai, S. D., Haines, B., Harvey, N., Moore, A. W., Owen, S., & Weiss, J. P. (2010). Single receiver phase ambiguity resolution with GPS data. *Journal of Geodesy*, *84*(5), 327–337.
- Boehm, J., Werl, B., & Schuh, H. (2006). Troposphere mapping functions for GPS and very long baseline interferometry from European Centre for Medium-Range Weather Forecasts operational analysis data. *Journal of Geophysical Research*, *111*(B2). <https://doi.org/10.1029/2005JB003629>
- Lyard, F., Lefevre, F., Letellier, T., & Francis, O. (2006). Modelling the global ocean tides: Modern insights from FES2004. *Ocean Dynamics*, *56*(5–6), 394–415.
- Rebischung, P., Griffiths, J., Ray, J., Schmid, R., Collilieux, X., & Garayt, B. (2012). IGS08: The IGS realization of ITRF2008. *GPS Solutions*, *16*(4), 483–494.
- Zumberge, J. F., Heftin, M. B., Jefferson, D. C., Watkins, M. M., Webb, F. H., Heflin, M. B., et al. (1997). Precise point positioning for the efficient and robust analysis of GPS data from large networks. *Journal of Geophysical Research*, *102*(B3), 5005–5017. <https://doi.org/10.1029/96JB03860>